The limited resolution of the $n = 1$ and $n = 2$ Rabi oscillations is a result of the cumulative effect of velocity and detuning fluctuations, a 3–5% miscount rate in the state-selective detectors and detector dark counts. The presence of number states, however, can be determined independently of the resolution because the only important factor is the accumulated Rabi phase of the probe atom as it passes through the cavity. The data for the $n = 1$ and $n = 2$ Rabi oscillations were evaluated considering possible disturbances by trapping states.

We now calculate the dissipation of the field before detection in order to determine the influence of dissipation. For these simulations we make two idealizing assumptions: thermal photons are only taken into account for the long-term build-up of the cyclically steady state, and gaussian averaging over velocity spread of atoms is considered to be about 3%. Considered in the calculations are the exponential decays for the cavity field during the pulse when either one photon (for $n = 1$) or two photons were deposited one by one (for $n = 2$) changing the photon number distribution. The simulations also average over the poissonian arrival times of the atoms. The details of this calculation will be discussed elsewhere (B. T. H. V. *et al*., manuscript in preparation). The results of these calculations are compared to the experimental results in Fig. 4a–f.

As dissipation is the dominant loss mechanism, it is interesting to compare the purity of the number states generated by the current method with that expected for trapping states (Fig. 4g–i). The agreement of the purity of the number states is very good. The trapping-state photon distribution is generated in the steady state, which means that whenever the loss of a photon occurs the next incoming atom will restore the old field with a high probability. The non-zero amplitudes of the states $|0\rangle$ in Fig. 4h and $|1\rangle$ in Fig. 4i are due to dissipative losses before restoration of a lost photon, which is not replaced immediately but after a time interval dependent on the atom flux. The atom rate used in these calculations was 25 atoms per cavity decay time, or an average delay of 1 ms. This can be compared to the delay between the preparation and probe atoms in the present experiment. In the steady-state simulation loss due to cavity decay determines the purity of the number state; in the limit of zero loss the state measurement is perfect. We conclude that dissipative loss due to cavity decay in the delay to a probe atom largely determines the measured deviation from a pure number state. The thermal field also influences the photon distribution. The nature of the selection process in the current experiment means that we can reduce the influence of the thermal field by only performing measurements of the field state after a trigger of n ground state atoms. Hence, the state of the field is well known. The steady-state simulation was therefore performed for a temperature of 100 mK, which makes the influence of the thermal field in the steady-state correspondingly low.

The fact that number states can be readily created presents many opportunities. For example, in connection with the investigation of quantum information, the decoherence of 'Schrödinger cat' states can be largely attributed to dissipation. The very low influence of dissipation in this experiment provides an excellent environment for investigating decoherence and non-local quantum phenomena such as entanglement of atoms. □

Received 26 April; accepted 2 December 1999.

1. Leibfried, D. *et al.* Experimental determination of the motional quantum state of a trapped atom. *Phys. Rev. Lett*. **77,** 4281–4285 (1996).
2. Hong, C. K. & Mandel, L. Experimental realization of a localized one photon state. *Phys. Rev. Lett.* **56,** 58–60 (1986).
3. Fearn, H. & Loudon, R. Theory of two-photon interference. *J. Opt. Soc. Am. B* **6,** 917–927 (1989).
4. Weidinger, M., Varcoe, B. T. H., Heerlein, R. & Walther, H. Trapping states in the micromaser. *Phys. Rev. Lett.* **82,** 3795–3798 (1999).
5. Maître, X. *et al.* Quantum memory with a single photon in a cavity. *Phys. Rev. Lett.* **79,** 769–772 (1997).
6. Englert, B. *et al.* Entangled atoms in micromaser physics. *Fortschr. Phys.* **46,** 897–926 (1998).
7. Nogues, G. *et al.* Seeing a single photon without destroying it. *Nature* **400,** 239–242 (1999).
8. Englert, B.-G., Sterpi, N. & Walther, H. Parity States in the one-atom maser. *Opt. Commun*. **100,** 526–535 (1993).
9. Rempe, G. & Walther, H. Sub-poissonian atomic statistics in a micromaser. *Phys. Rev. A* **42,** 1650–1655 (1990).
10. Rempe, G., Walther, H. & Klein, N. Observation of quantum collapse and revival in the one-atom maser. *Phys. Rev. A* **58,** 353–356 (1987).
11. Raithel, G., Benson, O. & Walther, H. Atomic interferometry with the micromaser. *Phys. Rev. Lett.* **75,** 3446–3449 (1995).
12. Benson, O., Raithel, G. & Walther, H. Quantum jumps of the micromaser field - dynamic behavior close to phase transition points. *Phys. Rev. Lett*. **72,** 3506–3509 (1994).
13. Filipowicz, P., Javanainen, J. & Meystre, P. Theory of a microscopic maser. *J. Opt. Soc. B* **34,** 3077–3087 (1986).
14. Cummings, F. W. & Rajagopal, A. K. Production of number states of the electromagnetic field. *Phys. Rev. A* **39** 3414–3416 (1989).
15. Jaynes, E. T. & Cummings, F. W. Quantum and semiclassical radiation theories. *Proc. IEEE* **51,** 89–109 (1963).
16. Meystre, P., Rempe, G. & Walther, H. Very-low temperature behavior of a micromaser. *Opt. Lett.* **13,** 1078–1080 (1988).
17. Krause, J., Scully, M. O. & Walther, H. State reduction and $|n\rangle$-state preparation of a high-Q micromaser. *Phys. Rev. A* **36,** 4547–4550 (1987).
18. Wehner, E., Seno, R., Sterpi, N., Englert, B.-G. & Walther, H. Atom pairs in the micromaser. *Opt. Commun*. **110,** 655–669 (1994).
19. Brune, M. *et al*. Quantum Rabi oscillation: A direct test of field quantisation in a cavity. *Phys. Rev. Lett*. **76,** 1800–1803 (1996).

Acknowledgements

We thank B.-G. Englert for the theoretical calculations of the cavity photon number and for many useful discussions.

Correspondence and requests for materials should be addressed to H. W. (e-mail: herbert.walther@mpq.mpg.de).

Imaging the effects of individual zinc impurity atoms on superconductivity in $Bi_2Sr_2CaCu_2O_{8+\delta}$

S. H. Pan*†, E. W. Hudson*, K. M. Lang*, H. Eisaki‡§, S. Uchida‡ & J. C. Davis*

* *Department of Physics, University of California, Berkeley, California 94720, USA*

‡ *Department of Superconductivity, University of Tokyo, Tokyo 113-8656, Japan*

§ *Department of Applied Physics, Stanford University, Stanford, California 94305, USA*

Although the crystal structures of the copper oxide high-temperature superconductors are complex and diverse, they all contain some crystal planes consisting of only copper and oxygen atoms in a square lattice: superconductivity is believed to originate from strongly interacting electrons in these CuO_2 planes. Substituting a single impurity atom for a copper atom strongly perturbs the surrounding electronic environment and can therefore be used to probe high-temperature superconductivity at the atomic scale. This has provided the motivation for several experimental[1–8] and theoretical studies[9–20]. Scanning tunnelling microscopy (STM) is an ideal technique for the study of such effects at the atomic scale, as it has been used very successfully to probe individual impurity atoms in several other systems[21–25]. Here we use STM to investigate the effects of individual zinc impurity atoms in the high-temperature superconductor $Bi_2Sr_2CaCu_2O_{8+\delta}$. We find intense quasiparticle scattering resonances[26] at the Zn sites, coincident with strong suppression of superconductivity within ~15 Å of the scattering sites. Imaging of the spatial dependence of the quasiparticle density of states in the vicinity of the impurity atoms reveals the long-sought four-fold symmetric quasiparticle 'cloud' aligned with the nodes of the *d*-wave superconducting gap which is believed to characterize superconductivity in these materials.

† Present address: Department of Physics, Boston University, Boston, Massachusetts 02215, USA.

We have previously reported that STM spectroscopy of nominally undoped $Bi_2Sr_2CaCu_2O_{8+\delta}$ (BSCCO) crystals revealed atomic-scale regions having a relatively high density of low-energy quasiparticle states[26]. The spatial and spectroscopic characteristics of these states were consistent with theories of quasiparticle scattering from atomic-scale impurities in a *d*-wave superconductor[10,12,13]. However, the location in the crystal and the identity of these scattering centres was unknown. Furthermore, another STM experiment showed that introduction of atomic-scale defects onto the BSCCO surface also generated low-energy quasiparticle states[27]. Recently, high-quality single crystals with controlled impurities have become available for STM studies. Here we describe the first use, to our knowledge, of STM to study local effects due to impurity atoms of known identity and crystal location in a high-T_c superconductor.

Our work focuses on Zn impurity atoms in BSCCO because they create strongly altered bulk superconducting properties[1–4] and very unusual spectroscopic effects[5–8]. We use a home-built, low-temperature STM which has several unique features particularly suited to the study of high-temperature superconductors[26]. The samples used are $Bi_2Sr_2Ca(Cu_{1-x}Zn_x)_2O_{8+\delta}$ single crystals grown by the floating zone method[28], with $x = 0.6\%$. They have been characterized to have a T_c of 84 K with a transition width of 4 K. These crystals are cleaved *in situ* at 4.2 K in cryogenic ultrahigh vacuum and are inserted into the STM immediately after cleavage.

A standard STM topographic image is first taken to determine the condition of the crystal surface, and a typical result is shown in Fig. 1a. A single crystal plane—believed to be usually the BiO layer with only the Bi atoms apparent in STM imaging—is exposed. The indistinguishability of these surfaces from those of non Zn-doped BSCCO[26,27] is consistent with the fact that Zn dopant atoms do not reside at the BiO plane but rather at the Cu sites two layers below the surface.

To search for low-energy quasiparticle states associated with the Zn atoms, we next map the differential tunnelling conductance at zero sample bias, for a larger area of the surface. Because at any point the local density of states (DOS) is proportional to the differential conductance, this results in a map of the zero-energy DOS at the surface. Figure 1b is a typical DOS-map of a 500×500 Å region of the same surface as shown in Fig. 1a, and the overall dark background is indicative of a very low quasiparticle DOS near the Fermi level. This is as expected for a superconductor far below T_c. Remarkably, however, there are a number of randomly distributed bright sites corresponding to areas of high DOS, each with a distinct four-fold symmetric shape and the same relative orientation.

Further investigation of these bright sites reveals very significant differences between conductance spectra taken exactly at their centres and spectra taken at usual superconducting regions of the sample (dark areas in Fig. 1b). In Fig. 2 we show a comparison between two such spectra, from which several observations can be made. First, the spectrum at the centre of a bright site has a very strong intra-gap DOS peak, whose magnitude can be up to six times

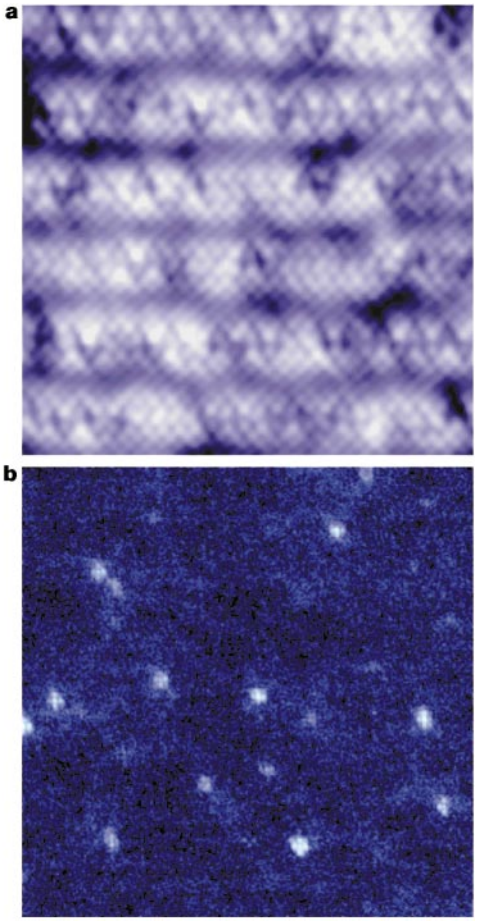

Figure 1 Topographic image and associated low-energy DOS-map of the surface layer (BiO) of a cleaved single crystal of BSCCO. **a**, Topographic image (150 × 150 Å) of the surface BiO plane which is exposed after cleavage of a Zn-BSCCO single crystal. The atoms are displaced from their ideal square lattice sites, forming a supermodulation along the crystal **b**-axis. The image of this surface is indistinguishable from those of non Zn-doped BSCCO. (T = 4.2 K, I = 100 pA, V_{sample} = −100 mV). **b,** A zero-bias differential tunnelling conductance map (500 × 500 Å), taken on a larger area of the same surface and with the same orientation as that shown in **a**. Because the differential tunnelling conductance dI/dV is proportional to the sample DOS, this is also a map of the quasiparticle DOS at the Fermi energy (V_{sample} = 0). Most of the image appears dark, which is indicative of a very low density of quasiparticles at the Fermi level. The Zn scattering sites appear as bright regions ~15 Å in extent, each clearly exhibiting a cross-shaped four-fold symmetric structure. Note that the orientations of all these cross-shaped features are the same. To acquire this image we operated at 4.2 K, set a 1 GΩ junction resistance (I = 200 pA, V_{sample} = −200 mV), and measure the tunnelling conductance with a standard low-frequency a.c. lock-in technique ($A_{modulation}$ = 500 μV_{rms}, $f_{modulation}$ = 447.3 Hz). The surface area shown in **a** is at the top centre of the DOS map in **b**.

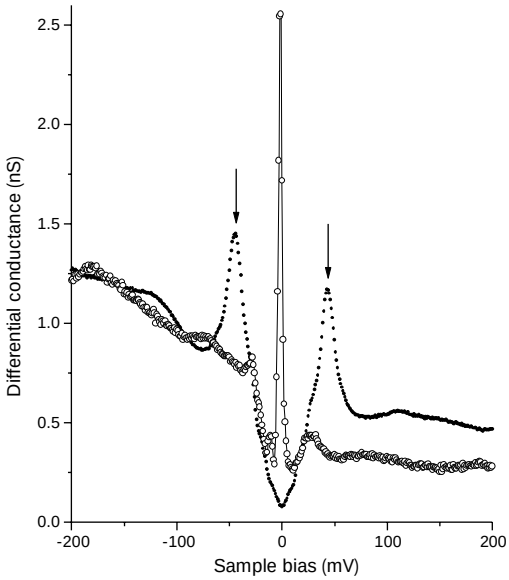

Figure 2 Two tunnelling spectra measured on the same surface shown in Fig. 1. Shown are differential tunnelling conductance spectra taken at two different locations on the Zn-BSCCO crystal. The spectrum of a 'usual' superconducting region of the sample, where Zn scatterers are absent (dark in Fig. 1b), is shown as filled circles. The superconducting coherence peaks are indicated by the arrows. The data shown as open circles, with an interpolating fine solid line, are the spectrum taken exactly at the centre of a bright scattering site. It shows both the intense scattering resonance peak centred at Ω = −1.5 meV, and the very strong suppression of both the superconducting coherence peaks and gap magnitude at the Zn site.

greater than the normal-state conductance. Second, these peaks occur at typical values of quasiparticle energy (as measured from the Fermi level) of $\Omega = -1.5 \pm 0.5$ meV. Third, at these sites the superconducting coherence peaks (identified by the arrows in Fig. 2) are strongly suppressed, indicating the almost complete destruction of superconductivity. All of these phenomena are among the theoretically predicted characteristics of a very strong quasiparticle scattering resonance at a single impurity atom in a *d*-wave superconductor[12,13,15,16,18,20].

To identify the source of these resonances, we next acquire simultaneous pairs of high-resolution topographic images and resonant-energy DOS-maps, centred on the resonance sites. Comparison between each topograph/DOS-map pair shows that the centre of a scattering resonance always coincides with the site of a surface Bi atom, as shown for example in Fig. 3a and b. From the known crystal structure of BSCCO, a Cu site where the Zn dopant atom could reside is directly below each exposed Bi atom, and separated from it by the intervening SrO_2 layer. Furthermore, the characteristic spatial features of the resonance (as shown for example in Fig. 3b) have never been observed in non-Zn-doped BSCCO crystals. Finally, the density of the observed scattering resonance sites is about $x = 0.2\%$, in reasonable agreement with the nominal Zn doping concentration, and no population of weak scatterers similar to those in ref. 26 is observed in these Zn-BSCCO crystals. We therefore attribute the observed very strong resonances to quasiparticle scattering at the Zn impurity atoms.

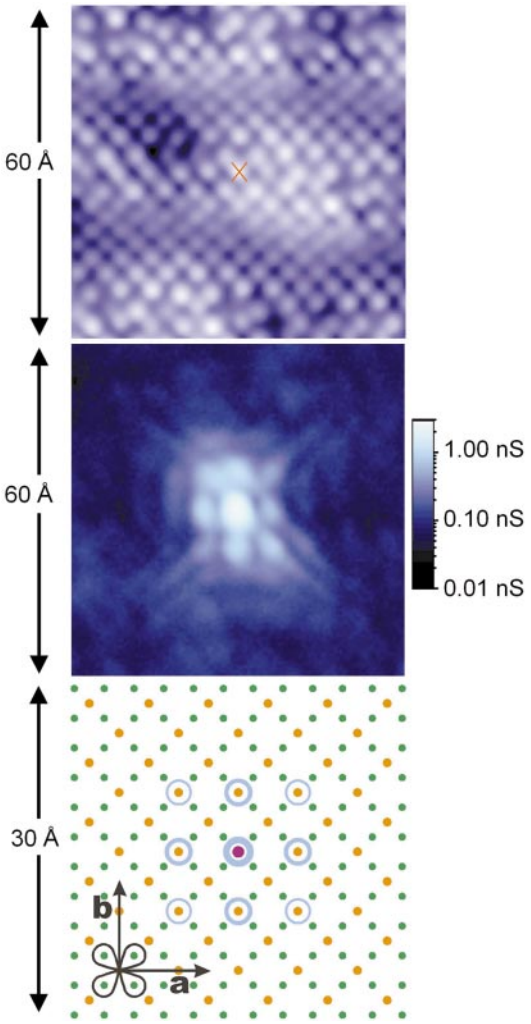

Figure 3 Relationship between the position of the Bi atoms on the crystal surface, the resonant DOS structure at the Zn atom, and the position of the Cu and O atoms in the superconducting plane two layers below. **a** and **b** are simultaneously acquired, 60 × 60 Å, high-spatial-resolution images of the topography and the differential conductance at $V_{sample} = -1.5$ mV. The bright centre of the scattering resonance in **b** coincides with the position of the Bi atom marked by an X in **a**. Note that **b** uses a logarithmic scale of intensity as the features at largest distances from the Zn site are more than two orders of magnitude weaker than the resonance peak. The inner bright cross is oriented with the nodes of the *d*-wave gap (as indicated schematically in **c**). The weaker outer features, including the ~30-Å-long ''quasiparticle beams'' at 45° to the inner cross, are oriented with the gap maxima. **c,** A 30 × 30 Å schematic representation of the square CuO_2 lattice, which is located two layers below the exposed surface BiO plane, showing its relative orientation to the BiO surface in **a**. The Cu atoms are indicated as orange circles and the O atoms as green circles, while the Zn scatterer (in purple) is at the central point. The crystal **a**-axis and **b**-axis orientations, and the orientations of the maxima and nodes of the *d*-wave superconducting gap, as measured by ARPES experiments, are also shown. The location of the maxima in the DOS, as measured from **b**, are shown schematically as open blue circles surrounding the atomic sites with which they appear to be associated. The intensity of the DOS at these sites is shown schematically by the thickness of the line forming these circles.

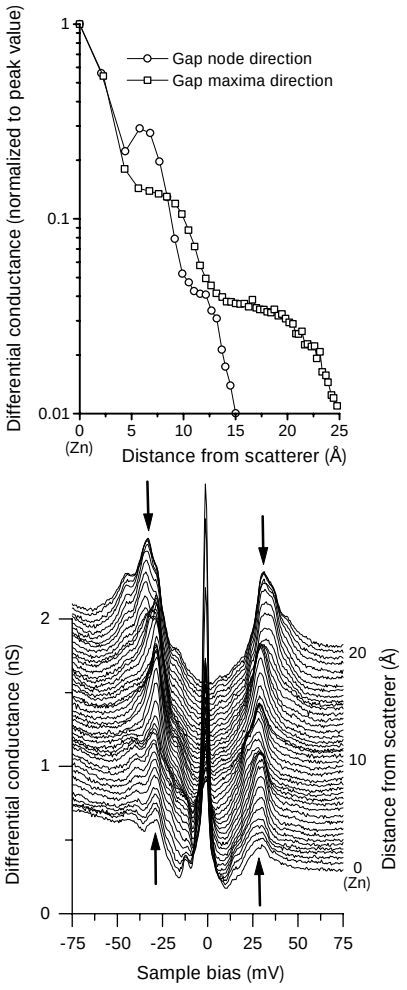

Figure 4 Evolution of the differential tunnelling conductance at the resonance energy, and the full conductance spectrum, with distance from the Zn site. **a,** Differential tunnelling conductance (normalized to the peak value) versus distance *r* from the centre of a Zn scatterer, along the **a**-axis or **b**-axis (gap-node) directions (shown as open circles) and along the Cu–O bond (gap-maxima) directions (shown as open squares). Each data point is the local DOS at distance *r* averaged over an inclusive angle of 10° around the given directions. **b,** Waterfall plot of a series of tunnelling spectra taken on a line from the scatterer along the **b**-axis direction in 0.5-Å steps. This clearly shows the suppression of the coherence peaks (whose absence at the Zn scatterer is indicated by upward pointing arrows), and recovery of the superconductivity (along with the coherence peaks whose presence is indicated by downward pointing arrows) within a distance of ~ 15 Å from the scattering site.

The DOS-maps at Zn scattering resonance sites show complex structures consisting of spatial elements whose DOS varies over two orders of magnitude. To show these elements in full detail, Fig. 3b is presented in a logarithmic intensity scale. Many features are apparent in this representation. In addition to the central bright spot, we see that a dominant feature is a relatively bright cross-shaped region aligned along the crystal **a**- and **b**-axes, and extending to a radius of about 10 Å. Concentric with this bright cross, and rotated 45° degrees relative to it, another cross-shaped feature with considerably lower intensity extends to approximately 30 Å from the centre.

The quasiparticle DOS at the resonance energy does not decay monotonically with distance r from the scatterer but rather oscillates, producing local minima and maxima in the DOS-map. Analysis of the correspondence of DOS local maxima in Fig. 3b, with the simultaneously imaged atomic positions in Fig. 3a, indicates that they coincide with positions of only some of the atomic sites near the scattering centre. To help clarify the spatial register of these DOS oscillations to the crystal, we show schematically in Fig. 3c the positions of the Cu and O atoms in the CuO_2 plane with the positions of DOS local maxima at the BiO plane overlaid as blue circles. Also shown are the orientations of the crystal **a**- and **b**-axes, and that of the d-wave gap nodes as determined by angle-resolved photoemission spectroscopy (ARPES)[29]. The positions of the four nearest-neighbour Cu atoms to the Zn have no DOS local maxima associated with them. On the other hand, the positions of the eight second-nearest-neighbour and third-nearest-neighbour Cu atoms coincide with local maxima in the DOS image, and appear to form a 'box' around the scatterer (Fig. 3b).

In Fig. 4a we plot the normalized DOS at the resonance energy as a function of r along both the gap-node and gap-maxima directions. Due to the strength of the oscillations it is difficult to identify, for comparison with theory[12,13,19,20], a power law governing the fall-off of the DOS with r in these directions. However, the rate of decay is clearly faster in the gap-node directions, while towards the gap maxima weak "quasiparticle beams" are apparent up to 30 Å from the scatterer.

The Zn impurity atom locally affects not only the low-energy DOS, but also features at the gap energy scale. Its effect on the magnitude of the coherence peaks, and on the width of the superconducting gap, is shown in Fig. 4b, which is a plot of the measured evolution of the complete DOS spectrum as the tip of the STM is moved away from the scattering site along the **b**-axis. The superconducting coherence peaks are strongly suppressed at the Zn scattering site, and recover to their usual value over a distance of about 15 Å.

We have found that all the above phenomena are characteristic of large numbers of scattering sites in several Zn-doped BSCCO crystal samples. When compared to the previous observations at the weaker scatterers of unknown identity[26], the Zn resonances are clearly much stronger, which in turn allows us to determine their detailed spatial structure with far greater resolution.

Some observations at the Zn scatterers are in excellent agreement with theoretical predictions. For example, theoretical proposals that quasiparticle scattering resonances, and localized impurity states, could be created by individual impurity atoms in a d-wave superconductor[10–13,15–20] are here shown to be correct. The strength of the scattering leading to these resonances, in terms of a phase shift δ_0, may be calculated, in the context of refs 12 and 13, using the ratio of the resonance energy Ω to the energy gap Δ_0:

$$\left|\frac{\Omega}{\Delta_0}\right| \approx \frac{\pi c/2}{\ln(8/\pi c)} \qquad (1)$$

where $c = \cot(\delta_0)$. Using an average gap value (away from the impurities) of $\Delta_0 = 45$ mV and $\Omega = -1.5$ mV, we obtain a phase shift of 0.48π. This confirms that scattering from Zn is very close to the unitary limit ($\delta_0 = \pi/2$)[9–20]. The predicted particle–hole symmetry breaking at a non-magnetic impurity atom scattering resonance[12,13,20] is directly confirmed. The predicted four-fold symmetry in the spatial distribution of the DOS near an impurity atom[10,12,13,20], and its alignment with the d-wave gap nodes, are also clearly observed.

Our measurements also provide microscopic validation for models proposed to explain the results of several previous experiments. A proposal that superfluid density reductions can be explained by non-superconducting regions of area $\pi\xi^2$ where ξ is the coherence length around each impurity atom[5](the 'Swiss cheese' model) is directly validated, both qualitatively and quantitatively, by the suppression of superconductivity near the Zn site shown in Fig. 4b. The strong non-zero energy quasiparticle DOS at the impurity atoms, which was postulated to explain infrared spectroscopy results[6], is also directly confirmed by the results shown in Fig. 2.

Despite this consistency between previous theoretical and experimental results and our measurements, we have also observed several unexpected phenomena. These include the extended "quasiparticle beams" oriented with the gap maxima, and the local maxima in the DOS associated with specific atomic sites. These phenomena suggest that to fully explain our results, a more sophisticated model is needed, which considers effects such as the symmetry of the interlayer tunnelling matrix element ($t_\perp$) (ref. 30), the band structure[17,19], or local magnetic moments at the Zn sites[31,32].

For example, the angular dependence of the interlayer tunnelling matrix element, which connects the BiO surface layer to the CuO_2 plane, may partially explain one of the unexpected observations. This matrix element is believed to have the same symmetry as the d_{x2-y2} order-parameter[30], and thus would reduce the tunnelling signal for states along the gap-node directions and enhance it for states towards the gap-maxima. This would result in an apparent rapid decay of the DOS in the gap-node directions and an apparent long extension of states oriented towards the gap maxima, which is consistent with our observations. In fact, within this framework, the clear observation at the surface of the cross-shaped DOS towards the gap nodes indicates that this characteristic feature would be even more dominant in the CuO_2 plane. However, the register of the DOS to specific atoms cannot be explained by effects of $t_\perp$. In particular, no DOS maxima are associated with the nearest-neighbour Cu sites although $t_\perp$ would apparently allow local maxima at these locations.

Finally, the reported quasiparticle scattering spectroscopy and DOS imaging at individual impurity atoms in the copper oxides not only reveals new information on electronic impurity states in high-temperature superconductors but also opens a new avenue for research into these important materials. □

Received 1 September; accepted 3 December 1999.

1. Maeda, A., Yabe, T., Takebayashi, S., Hase, M. & Uchinokura, K. Substitution of 3d metals for Cu in $Bi_2(Sr_{0.6}Ca_{0.4})_3Cu_2O_y$ *Phys. Rev. B* **41,** 4112–4117 (1990).
2. Ishida, K. *et al.* Gapless superconductivity in Zn-doped $YBa_2Cu_3O_7$ studied by Cu NMR and NQR. Possibility of d-wave superconductivity in high-T_c oxides *Physica C* **179,** 29–38 (1991).
3. Bonn, D. A. *et al.* Comparison of the influence of Ni and Zn impurities on the electromagnetic properties of $YBa_2Cu_3O_{6.95}$. *Phys Rev. B* **50,** 4051–4063 (1994).
4. Fukuzumi, Y., Mizuhashi, K., Takenaka, K. & Uchida, S. Universal superconductor-insulator transition and T_c depression in Zn-substituted high-T_c cuprates in the underdoped regime. *Phys. Rev. Lett.* **76,** 684–687 (1996).
5. Nachumi, B. *et al.* Muon spin relaxation studies of Zn-substitution effects in high-T_c cuprate superconductors *Phys. Rev. Lett.* **77,** 5421–5424 (1996).
6. Basov, D.N., Dabrowski, B. & Timusk, T. Infrared probe of transition from superconductor to nonmetal in $YBa_2(Cu_{1-x}Zn_x)_4O_8$ *Phys. Rev. Lett.* **81,** 2132–2135 (1998).
7. White, P.J *et al.* Zn impurities in $Bi_2Sr_2Ca(Cu_{1-x}Zn_x)_2O_{8+\delta}$ – electronic structure evolution. Preprint cond-mat/9901349 at ⟨http://xxx.lanl.gov⟩ (1999).
8. Fong, H.F *et al.* Effect of nonmagnetic impurities on the magnetic resonance peak in $YBa_2Cu_3O_7$. *Phys. Rev. Lett.* **82,** 1939–1942 (1999).
9. Lee, P. A. Localized states in a d-wave superconductor *Phys. Rev. Lett.* **71,** 1887–1890 (1993).
10. Byers, J.M., Flatté, M.E. & Scalapino, D.J. Influence of gap extrema on the tunneling conductance near an impurity in an anisotropic superconductor *Phys. Rev. Lett.* **71,** 3363–3366 (1993).
11. Sun, Y. & Maki, K. Impurity effects in d-wave superconductors *Phys. Rev. B* **51,** 6059–6063 (1995).
12. Balatsky, A.V., Salkola, M.I. & Rosengren, A. Impurity-induced virtual bound states in d-wave superconductors *Phys. Rev. B* **51,** 15547–15551 (1995).
13. Salkola, M.I., Balatsky, A.V. & Scalapino, D.J. Theory of scanning tunneling microscopy probe of impurity states in a d-wave superconductor *Phys. Rev. Lett.* **77,** 1841–1844 (1996).
14. Hirschfeld, P.J. & Puttika, W.O. Theory of thermal conductivity in $YBa_2Cu_3O_{7-\delta}$ *Phys. Rev. Lett.* **77,** 3909–3912 (1996).

15. Franz, M., Kallin, C. & Berlinsky, A.J. Impurity scattering and localization in *d*-wave superconductors *Phys. Rev. B* **54,** R6897–R6900 (1996).
16. Salkola, M.I. & Schrieffer, J.R. Unusual states of inhomogeneous $d_{x2-y2} + id_{xy}$ superconductors *Phys. Rev. B* **58,** R5952–R5955 (1998).
17. Atkinson, W.A. & MacDonald, A.H. Visualizing quasiparticle scattering resonances *Science* **285,** 57–58 (1999).
18. Tsuchiura, H., Tanaka, Y., Ogata, M. & Kashiwaya, S. Quasiparticle properties around a nonmagnetic impurity in the superconducting state of the two-dimensional *t-J* model. *J. Phys. Soc. Jpn* **68,** 2510–2513 (1999).
19. Flatte, M.E. & Byers, J.M. Local electronic structure of defects in superconductors *Solid State Phys.* **52,** 137–228 (1999).
20. Salkola, M.I., Balatsky, A.V. & Schrieffer, J.R. Spectral properties of quasiparticle excitations induced by magnetic moments in superconductors *Phys. Rev. B* **55,** 12648–12661 (1997).
21. Crommie, M.F., Lutz, C.P. & Eigler, D.M. Imaging standing waves in a two-dimensional gas *Nature* **363,** 524–527 (1993).
22. Zheng, J.F *et al*. Scanning tunneling microscopy studies of Si donors (Si_{Ga}) in GaAs. *Phys. Rev. Lett.* **72,** 1490–1493 (1994).
23. Yazdani, A., Jones, B.A., Lutz, C.P., Crommie, M.F. & Eigler, D.M. Probing the local effects of magnetic impurities on superconductivity *Science* **275,** 1767–1770 (1997).
24. Madhavan, V., Chen, W. Jamneala, T., Crommie, M.F. & Wingreen, N.S. Tunneling into a single magnetic atom: spectroscopic evidence of the Kondo resonance *Science* **280,** 567–569 (1998).
25. Wittneven, Chr., Dombrowski, R., Morgenstern, M. & Wiesendanger, R. Scattering states of ionized dopants probed by low temperature scanning tunneling spectroscopy *Phys. Rev. Lett.* **81,** 5616–5619 (1998).
26. Hudson, E.W., Pan, S.H., Gupta, A.K., Ng, K.-W. & Davis, J.C. Atomic-scale quasiparticle scattering resonances in $Bi_2Sr_2CaCu_2O_{8+\delta}$ *Science* **285,** 88–91 (1999).
27. Yazdani, A., Howald, C.M., Lutz, C.P., Kapitulnik, A. & Eigler, D.M. Impurity-induced bound excitations on the surface of $Bi_1Sr_2CaCu_2O_8$ *Phys. Rev. Lett.* **83,** 176–179 (1999).
28. Motohira, N., Kuwahara, K., Hasegawa, T., Kishio, K. & Kitazawa, K. Single crystal growth of $Bi_2Sr_2Ca_{n-1}Cu_nO_y$ superconductors by the floating zone method *J. Ceram. Soc. Jpn* **97,** 1009–1014 (1989).
29. Wells, B.O. *et al*. Evidence for k-dependent, in-plane anisotropy of the superconducting gap in $Bi_2Sr_2CaCu_2O_{8+\delta}$. *Phys. Rev. B* **46,** 11830–11834 (1992).
30. Andersen, O. K., Jepsen, O., Liechtenstein, A. I. & Mazin, I. I. Plane dimpling and saddle-point bifurcation in the band structures of optimally doped high-temperature superconductors: a tight-binding model. *Phys. Rev. B* **49,** 4145–4157 (1994).
31. Mahajan, A.V., Alloul, H., Collin, G. & Marucco, J.F. ^{89}Y NMR probe of Zn induced local moments in $YBa_2(Cu_{1-y}Zn_y)_3O_{6+x}$ *Phys. Rev. Lett.* **72,** 3100–3103 (1994).
32. Nagaosa, N. & Lee, P.A. Kondo effect in high-T_c cuprates. *Phys. Rev. Lett.* **79,** 3755–3758 (1997).

Acknowledgements

We thank A. Balatsky, D. Bonn, M. Crommie, M. Flatté, M. Franz, S. Kashiwaya, A. de Lozanne, A. MacDonald, V. Madhavan, M. Ogata, J. Orenstein, D. J. Scalapino, Z.-X. Shen, Y. Tanaka and D. van der Marel for conversations and communications. This work was supported by the LDRD Program of the Lawrence Berkeley National Laboratory under contract to the Department of Energy, by the D. & L. Packard Foundation, by an IBM predoctoral fellowship (K.M.L.), by Grant-in-Aid for Scientific Research on Priority Area (Japan), and by a COE grant from the Ministry of Education, Japan.

Correspondence and requests for materials should be addressed to J.C.D. (e-mail: jcdavis@socrates.berkeley.edu).

High-efficiency fluorescent organic light-emitting devices using a phosphorescent sensitizer

M. A. Baldo*, M. E. Thompson† & S. R. Forrest*

** Center for Photonics and Optoelectronic Materials (POEM), Department of Electrical Engineering and the Princeton Materials Institute, Princeton University, Princeton, New Jersey 08544, USA*
† Department of Chemistry, University of Southern California, Los Angeles, California 90089, USA

To obtain the maximum luminous efficiency from an organic material, it is necessary to harness both the spin-symmetric and anti-symmetric molecular excitations (bound electron–hole pairs, or excitons) that result from electrical pumping. This is possible if the material is phosphorescent, and high efficiencies have been observed in phosphorescent[1,2] organic light-emitting devices[3]. However, phosphorescence in organic molecules is rare at room temperature. The alternative radiative process of fluorescence is more common, but it is approximately 75% less efficient, due to the requirement of spin-symmetry conservation[4]. Here, we demonstrate that this deficiency can be overcome by using a phosphorescent sensitizer to excite a fluorescent dye. The mechanism for energetic coupling between phosphorescent and fluorescent molecular species is a long-range, non-radiative energy transfer: the internal efficiency of fluorescence can be as high as 100%. As an example, we use this approach to nearly quadruple the efficiency of a fluorescent red organic light-emitting device.

Light is generated in organic materials from the decay of molecular excited states, also known as excitons. Understanding the properties and interactions of excitons is crucial to the design of efficient organic devices for use in displays, lasers and other illumination applications. For example, the spin-symmetry of an exciton determines its probability of radiative recombination and also its multiplicity. Spin-symmetric excitons with a total spin of $S = 1$ have a multiplicity of three and are known as triplets. Spin-antisymmetric excitons ($S = 0$) have a multiplicity of one and are known as singlets. During electrical excitation approximately one singlet exciton is created for every three triplet excitons[4], but because the ground state is typically also spin-antisymmetric, only relaxations of singlet excitons conserve spin and generate fluorescence. Usually the energy in triplet excitons is wasted; however, given some perturbation in symmetry, triplets may slowly radiatively decay, producing the delayed luminescence known as phosphorescence. Although it is often inefficient, phosphorescence may be enhanced if spin–orbit coupling mixes the singlet and triplet states, an effect often promoted by the presence of a heavy metal atom[5]. Indeed, phosphorescent dyes with these properties have demonstrated very high-efficiency electroluminescence[1,2].

Very few organic materials have been found to be capable of efficient room-temperature phosphorescence from triplets[1,2,6]. In contrast, many organic molecules exhibit fluorescence[7,8] and fluorescence is also unaffected by triplet–triplet annihilation, which degrades phosphorescent emission efficiency at high excitation densities[1]. Consequently, fluorescent materials are suited to many electroluminescent applications, particularly those such as passive matrix displays that require high excitation densities.

It is desirable therefore to find a process whereby triplets that are formed after electrical excitation are not wasted, but are instead transferred to the singlet excited state of a fluorescent dye. There are two mechanisms for triplet–singlet energy transfer from a donor molecule (D) to an acceptor (A). In Dexter transport[5], the exciton hops directly between molecules. This is a short-range process dependent on the overlap of molecular orbitals of neighbouring molecules. It also preserves the symmetry of the donor and acceptor pair[5]. Thus, a triplet–singlet energy transfer is not possible by a Dexter mechanism. A change in spin-symmetry is possible if the donor exciton breaks up and reforms on the acceptor by incoherent electron exchange[5]. However, this process is considered to be relatively unlikely as it requires the dissociation of the donor exciton, which in most molecular systems has a binding energy of ~1 eV.

The alternative mechanism is Förster energy transfer[5]. Here, molecular transition dipoles couple and exchange energy. The efficiency of energy transfer (η_{ET}) is:

$$\eta_{ET} = \frac{k_{ET}}{k_{ET} + k_R + k_{NR}} \quad (1)$$

Here k_{ET} is the rate of Förster energy transfer from D to A and k_R and k_{NR} are the radiative and non-radiative rates on the donor, respectively. From equation (1), energy transfer is efficient if $k_{ET} > k_R + k_{NR}$; however, in Förster's theory k_{ET} is proportional to the oscillator strength of the donor transition[5], as is k_R. Thus, η_{ET} is approximately independent of oscillator strength if $k_R \gg k_{NR}$, that is, if the donor is efficiently phosphorescent then it is possible to

